

**How turbulence regulates biodiversity in systems with cyclic competition**Daniel Grošelj,<sup>1</sup> Frank Jenko,<sup>1,2</sup> and Erwin Frey<sup>3</sup><sup>1</sup>*Max-Planck-Institut für Plasmaphysik, Boltzmannstraße 2, D-85748 Garching, Germany*<sup>2</sup>*Department of Physics and Astronomy, University of California, Los Angeles, California 90095-1547, USA*<sup>3</sup>*Arnold Sommerfeld Center for Theoretical Physics and Center for NanoScience, Department of Physics, Ludwig-Maximilians-Universität München, Theresienstraße 37, D-80333 München, Germany*

(Received 14 November 2014; published 16 March 2015)

Cyclic, nonhierarchical interactions among biological species represent a general mechanism by which ecosystems are able to maintain high levels of biodiversity. However, species coexistence is often possible only in spatially extended systems with a limited range of dispersal, whereas in well-mixed environments models for cyclic competition often lead to a loss of biodiversity. Here we consider the dispersal of biological species in a fluid environment, where mixing is achieved by a combination of advection and diffusion. In particular, we perform a detailed numerical analysis of a model composed of turbulent advection, diffusive transport, and cyclic interactions among biological species in two spatial dimensions and discuss the circumstances under which biodiversity is maintained when external environmental conditions, such as resource supply, are uniform in space. Cyclic interactions are represented by a model with three competitors, resembling the children's game of rock-paper-scissors, whereas the flow field is obtained from a direct numerical simulation of two-dimensional turbulence with hyperviscosity. It is shown that the space-averaged dynamics undergoes bifurcations as the relative strengths of advection and diffusion compared to biological interactions are varied.

DOI: [10.1103/PhysRevE.91.033009](https://doi.org/10.1103/PhysRevE.91.033009)

PACS number(s): 47.54.Fj, 87.23.Cc, 47.27.wj, 05.45.Xt

**I. INTRODUCTION**

Several studies have shown that biodiversity in spatially extended population models can sometimes be maintained even if only a single species is able to survive in the well-mixed system [1–8]. This is typically the case if the interactions among individuals are sufficiently local and the system does not display a clear competition hierarchy as in the case of cyclic interactions. Cyclic competitions have been frequently investigated in discrete lattice models with nearest-neighbor interactions, where the dispersal of individuals is local [1,2,4,7,9–17]. To demonstrate the approach to the well-mixed limit in these models one can either increase the effective range of interactions towards the total domain size [2,4] or explicitly consider individuals' mobility by allowing random exchange events among adjacent sites, which leads to diffusive transport in the continuum limit [7,12,13,16]. However, a significant part of life on Earth is represented by microorganisms dwelling in moving fluid environments, such as the Earth's oceans, where the dominant mechanism of transport is typically attributed to fluid turbulence [18–20]. The latter mechanism of microorganisms' transport was a source of inspiration for the work presented herein since, despite the fact that cyclic interactions are used as a paradigm to explain biodiversity, to our knowledge, only one previous study has considered spatial games with cyclic dominance in a fluid environment with mixing [6], and so far none has been devoted to the study of cyclic competitions in a turbulent flow. One of the most intriguing examples of biological communities without a clear competition hierarchy inhabiting turbulent aquatic environments is represented by marine phytoplankton species that typically compete for a limited number of natural resources [21,22]. Apart from marine ecosystems there also seems to be a growing interest for biodiversity in the atmosphere, although it remains an open question as to whether organisms found in the atmosphere can be regarded as an active ecosystem [23–25].

Fluid motion can have a profound effect on the time evolution of passively advected biological populations or chemical substances [3,26–29]. In particular, stirring by a fluid flow can lead to transitions between different dynamical regimes of reactive systems, mathematically described by the so-called reaction-diffusion-advection (RDA) equations [30–33]. From an ecological point of view, these transitions correspond to changes in relative species abundance and are therefore of crucial importance for studies of biodiversity in moving fluid environments. Here we demonstrate that, upon changing the relative strengths of advection and diffusion compared to biological interactions, a spatially extended population model with cyclic dominance experiences dramatic changes in its spatiotemporal dynamics. Distinct dynamical regimes of the system are manifested by a rich variety of phenomena such as rotating spiral waves, the emergence of periodic oscillations in relative species abundance, and transitions into absorbing states where only one species survives.

To shed some light on cyclic competitions in turbulent flows we adopt a minimal biological model with three competitors dominating each other in an analogous fashion as in the children's game of rock-paper-scissors, where rock crushes scissors, scissors cut paper, and paper covers rock. Known examples where cyclic dominance has been identified in interactions between three competitors include the mating strategies of lizards in the inner Coast Range of California [34], competitions between mutant strains of yeast [35], and bacterial strains of toxin-producing *Escherichia coli* [5,36,37]. In the spatially extended population model, the biological reactions are supplemented with diffusion terms and advection by a two-dimensional (2D) turbulent flow. Diffusion can be used either to represent random Brownian motion of the advected species or as a parametrization for turbulent transport below the model's resolution, i.e., at the scales where three-dimensional fluid motions become important [18,38]. Diffusion, however small it may be, in fact plays a crucial

role in the population dynamics of passively advected species because it enables particles in nearby fluid elements to come in contact and interact [29,39]. In cases where particle inertial effects or microorganism motility are considered important, the species may additionally come in contact due to an effective compressibility of the flow field [40–42]. In this study, however, these effects are neglected and the tracer velocity field is assumed to be incompressible.

It has been previously shown that cyclic interactions in combination with diffusion lead to self-organization of the three competitors into rotating spiral waves [7,12]. Turbulent advection in 2D flows is, on the other hand, known to produce sharp, patchy distributions of biological tracers [38,43–45]. Advective and diffusive transport in systems with cyclic competition are therefore drawn towards a complex interplay of diverse factors, exhibiting elements of competition as well as of cooperation. On one hand, these two processes work together to enhance the overall mixing rate, while, on the other hand, they represent two opposing mechanisms, favoring either sharp gradients in the subpopulation densities or smooth density profiles propagating in the form of traveling waves. Various relative strengths of turbulence compared to diffusion can be also viewed—in a more loose sense—as different compromises between the random Brownian and collective motions of individuals. Our model might therefore provide some general insight into situations where the motions of individuals are adequately described by a single, spatially correlated velocity field in the continuum limit. Apart from plankton species in the ocean, an interesting example belonging to this general class of biological systems is represented by swimming bacteria in dense suspensions [46] where the velocity correlation length was shown to depend mainly on the bacterial concentration [47]. We also note that the applications of this study concerning pattern formation in fluid flows are not limited to biological systems since qualitatively similar patterns to the ones observed in our model can also be reproduced with the celebrated Belousov-Zhabotinsky reaction [48–50].

In the ocean, advection is recognized as the dominant source of transport, and the biological interactions among planktonic organisms typically occur on similar time scales as horizontal mixing [38,43]. Nevertheless, in order to obtain a thorough understanding of the various physical processes involved, and due to possible applications of our work outside the field of marine ecology, we perform a comprehensive numerical analysis of our model over a wide range of relative advection as well as diffusion strengths compared to the biological interactions. All the available simulation results are then used to construct a rough nonequilibrium phase diagram of the spatiotemporal dynamics.

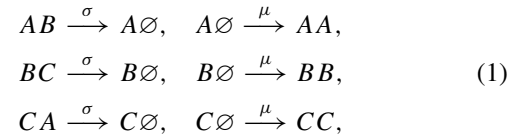
The remainder of this article is structured as follows. In Sec. II we present a set of rate equations describing cyclic interspecies interactions and give details regarding our 2D turbulence simulation before discussing the full set of RDA equations used to model the dynamics of the spatially extended system. In Sec. III we perform a detailed analysis of the numerical results. The complex spatiotemporal patterns are first inspected through snapshots of the solutions and by means of space-time autocorrelation functions. Afterwards, adopting a recently introduced method developed in the context of

interacting particle systems [51], we show that the most pronounced *qualitative* changes in the system’s spatiotemporal dynamics correspond to bifurcations of the space-averaged dynamics. The main conclusions are given in Sec. IV.

## II. MODEL

### A. Rate equations

We study a biological population comprised of three species  $A$ ,  $B$ , and  $C$  that cyclically dominate each other. In addition, the individuals from each subpopulation are able to reproduce if an empty spot  $\emptyset$  is available. The complete model composed of selection and reproduction processes is described by the following reaction scheme [12,17]:



where  $\sigma$  and  $\mu$  are the selection and reproduction rates, respectively. If the size of each subpopulation is macroscopically large, such that the relative fluctuations arising from stochastic effects are small, the system’s time evolution may be treated as deterministic, and the discrete distributions of individuals belonging to each species can be replaced by the mean densities  $a$ ,  $b$ , and  $c$  of subpopulations  $A$ ,  $B$ , and  $C$ , respectively. In the well-mixed limit, the mean population densities are governed by the following set of rate equations:

$$\begin{aligned} \partial_t a &= \mu a(1 - \rho) - \sigma a c, \\ \partial_t b &= \mu b(1 - \rho) - \sigma b a, \\ \partial_t c &= \mu c(1 - \rho) - \sigma c b, \end{aligned} \quad (2)$$

where  $\rho = a + b + c$  represents the total population density.

Equation (2) is a special case of a three-species population model first studied by May and Leonard [52]. For the above system, May and Leonard reported four nontrivial fixed points [52]: three single-species equilibrium points,  $(1,0,0)$ ,  $(0,1,0)$ , and  $(0,0,1)$ , and an unstable reactive fixed point,  $\frac{\mu}{3\mu+\sigma}(1,1,1)$ , where all three subpopulations coexist. The single-species fixed points correspond to absorbing states that can never be left by the system’s dynamics once they are reached. Solutions of Eq. (2) starting in the vicinity of the coexistence point form so-called *heteroclinic orbits* [52,53]: the trajectories  $[a(t), b(t), c(t)]$  spiral outwards from the coexistence point and come ever closer to the single-species equilibrium points but never converge to any of them. However, the time spent in the vicinity of the single-species fixed points increases proportionally with time. In consequence, one of the species will sooner or later dominate the other two over times which are much longer than any biological time scale of interest, even though there can be no winner in the strict limit  $t \rightarrow \infty$ . It should also be noted that any inclusion of (demographic) noise in the deterministic model (2) will inevitably lead to the complete extinction of all but one species in a finite time [54]. Reichenbach *et al.* [12] have investigated system (2) further and showed that all solutions of Eq. (2) decay onto a 2D invariant manifold (a subspace left invariant by the system’s time evolution), which contains all

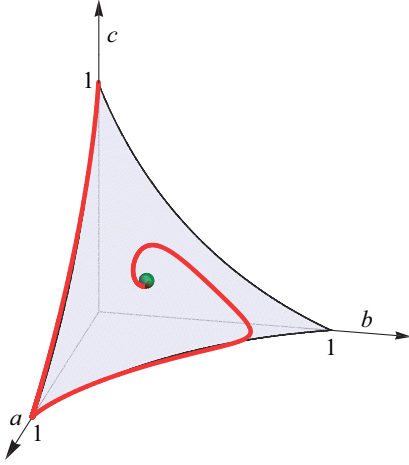


FIG. 1. (Color online) Evolution of subpopulation densities ( $a, b, c$ ) on the invariant manifold for equal selection and reproduction rates ( $\mu = \sigma$ ). The red (gray) curve shows a trajectory starting in the vicinity of the reactive fixed point.

four nontrivial fixed points. The invariant manifold together with an example of a phase-space trajectory starting in the vicinity of the reactive fixed point is shown in Fig. 1.

### B. Turbulence model

The turbulent velocity field is obtained from solutions of the incompressible, 2D Navier-Stokes equations with hyperviscosity and large-scale, random forcing. Real flows in nature are always, at least to some extent, three dimensional. However, the particular type of flow was primarily chosen to fit the needs of a model for the stirring of microorganisms by large-scale geophysical flows. These flows are strongly anisotropic due to geometrical constraints (large horizontal scale compared to the fluid's depth) and body forces acting on the fluid (Coriolis force, density stratification) and may be treated as 2D in the first approximation [55,56]. Fluid turbulence constrained to two spatial dimensions is characterized by many unique features such as an inverse cascade of kinetic energy to large scales, a cascade of enstrophy to small scales, and strong, long-lived vortices comparable to the size of the energy injection scale [57–59]. With the random forcing being concentrated at large scales, the flow field obtained from our simulations is smooth and limited to the direct 2D turbulence enstrophy cascade. Given the typical forcing scales in the ocean ( $\sim 50$  km) [3], large-scale forcing constrains the simulation domain size within the ocean mesoscale range, where horizontal advection is aptly described by the (standard) 2D Navier-Stokes equations [38]. We also note that similar modeling approaches have been used in many previous studies of population dynamics over large horizontal scales in the ocean [3,28,38,43–45].

In two dimensions the Navier-Stokes equations are most conveniently solved by integrating the vorticity equation [59]

$$\partial_t \omega + \mathbf{v} \cdot \nabla \omega = \mathcal{D} + \xi, \quad (3)$$

where  $\mathbf{v} = (v_x, v_y)$  is the 2D velocity field,  $\omega = \partial_x v_y - \partial_y v_x$  is the (scalar) vorticity,  $\mathcal{D}$  represents dissipation terms, and  $\xi$  is the external forcing. For the dissipation, we use a

sum of hyperviscosity and linear friction given by  $\mathcal{D} = \nu \Delta^3 \omega - \alpha \omega$ . The viscous term of the Navier-Stokes equations is frequently replaced by higher powers of the Laplacian in turbulence simulations because it is possible to achieve higher effective Reynolds numbers at a given spatial resolution in this way [60,61]. The second source of dissipation—the linear drag term—provides a large-scale energy sink, necessary to reach a statistically steady state in 2D turbulence simulations due to the flow of energy to large scales [58,59].

Equation (3) is solved with a pseudospectral method on a doubly periodic square domain at resolution  $768^2$  using the exponential time differencing fourth-order Runge-Kutta scheme [62] for the time integration. The random forcing is applied in spectral space by adapting a general forcing scheme for three-dimensional turbulence, introduced by Alvelius [63], to the 2D case. The forcing power spectrum is restricted to a narrow range of wave numbers with a peak at  $k_f = 2\pi/l_f$ , where  $l_f$  is a characteristic forcing length scale. Following the approach of Ref. [63], the time and length units of the simulation are fixed by the choice  $l_f \equiv 1$  and  $P \equiv 1$ , where  $P$  is the average external power input.

In the chosen units, the simulation domain edge length, hyperviscosity, and drag coefficient were set to  $L = 5$ ,  $\nu = 3 \times 10^{-13}$ , and  $\alpha = 0.13$ , respectively. Starting from an initial zero vorticity, Eq. (3) was integrated until a statistically steady state, characterized by a steady value of the total kinetic energy, was reached. The generated vorticity profile [Fig. 2(a)] was then used as the initial condition for vorticity in the simulations of cyclic competitions in a turbulent flow (see Sec. II C). To confirm that our numerical solution is consistent with well-known results from the literature, we computed the kinetic energy spectrum  $E(k)$  and the longitudinal velocity correlation function  $f(r) = \langle v_i(\mathbf{r}', t) v_i(\mathbf{r}' + r \hat{\mathbf{e}}_i, t) \rangle / \langle v_i^2 \rangle$  [Fig. 2(b)], where the brackets  $\langle \dots \rangle$  denote a space-time average, the index  $i$  represents the  $x$  or  $y$  direction, and  $\hat{\mathbf{e}}_i$  is the unit vector. We found  $f(r)$  to be a non-negative, monotonically decreasing function with a correlation length [the length  $\ell_c$  at which  $f(\ell_c) = \exp(-1)$ ] close to the forcing length scale. The estimated turbulence energy spectrum has a slope close to  $-3$  on the logarithmic graph, in the wave number range between the energy injection scale and hyperviscous dissipation scale. These results are in good agreement with theoretical predictions [57,58] and other numerical simulations [60,64].

### C. The spatially extended population model

In the spatially extended model, we combine the differential equations for species competition (2) and the turbulence model (3) into a set of RDA equations for the subpopulation densities  $a(\mathbf{r}, t)$ ,  $b(\mathbf{r}, t)$ ,  $c(\mathbf{r}, t)$ :

$$\begin{aligned} \partial_t a + \mathbf{v} \cdot \nabla a &= \mu a(1 - \rho) - \sigma a c + D \Delta a, \\ \partial_t b + \mathbf{v} \cdot \nabla b &= \mu b(1 - \rho) - \sigma b a + D \Delta b, \\ \partial_t c + \mathbf{v} \cdot \nabla c &= \mu c(1 - \rho) - \sigma c b + D \Delta c, \end{aligned} \quad (4)$$

where  $D$  is the diffusion constant and the flow field  $\mathbf{v}(\mathbf{r}, t)$  is determined at each time instant from Eq. (3).

The corresponding discretized version of system (4) as well as the continuous model have been extensively studied by Reichenbach *et al.* [7,12,65] for the case with no fluid

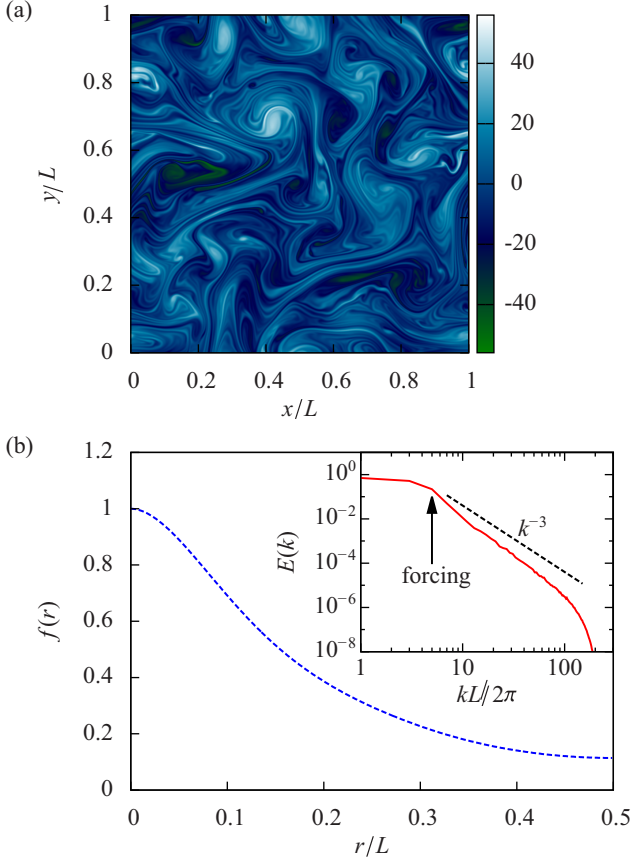


FIG. 2. (Color online) Results of the 2D turbulence simulation. (a) Snapshot of the vorticity field in a statistically steady turbulent state. (b) Longitudinal velocity correlation function. The inset shows the turbulence energy spectrum.

flow. The authors of Refs. [7,12,65] have shown that mobile individuals exhibiting cyclic dominance are able to coexist up to some critical value of species mobility (characterized by an effective diffusion constant in the continuum limit). Within the coexistence phase the fields  $a(\mathbf{r},t)$ ,  $b(\mathbf{r},t)$ , and  $c(\mathbf{r},t)$  self-organize—in two dimensions—into rotating spiral waves. As the species mobility increases, the spirals' wavelength grows proportionally to  $\sqrt{D}$  until the patterns outgrow the system size. The state in which spirals are absent corresponds to the well-mixed system (2) where only one subpopulation survives. Taking into account the main features of the reaction-diffusion part of Eq. (4), the natural time and length scale of the spatially extended model appear to be the spirals' rotation period  $T_0(\mu, \sigma)$  and the linear size of the simulation domain  $L$ . We shall make use of these units in the following analysis of our numerical results. It is also worth emphasizing that  $T_0$  is uniquely determined by  $\mu$  and  $\sigma$  alone [12], even though rotating spirals can only emerge in the presence of diffusion.

For a given type of 2D flow and for a fixed ratio  $\sigma/\mu$ , the solutions of Eq. (4) are characterized by two dimensionless parameters, which can be constructed by assigning a characteristic time scale to each of the three physical phenomena (reactions, diffusion, and advection) and comparing these scales to each other. Here we choose to analyze our results

in terms of the parameters

$$\text{Da} = \tau_f/\tau_r \quad \text{and} \quad K_d = \tau_d/\tau_r, \quad (5)$$

where  $\tau_r$ ,  $\tau_d$ , and  $\tau_f$  are a characteristic reaction, diffusion, and flow time scale, respectively. The ratio  $\text{Da}$  is known in literature as the *Damköhler number* [29]. We adopt a common definition for the flow time scale given by  $\tau_f = \ell_f/u$ , where  $u$  is the root-mean-square velocity of the flow [29,44]. For  $\tau_r$ , we use the definition  $\tau_r = T_0$  because this appears to be the slowest reaction time scale of Eq. (4), and it is reasonable to expect that the reactions will balance turbulent advection only when the slowest reaction time scale is able to keep up with the flow. We estimated the spirals' rotation period from simulation runs performed with  $\mathbf{v}(\mathbf{r},t) = 0$  and found  $T_0 \approx 61.5/\mu$  for  $\mu = \sigma$ , which is in good agreement with Reichenbach *et al.* [12]. The diffusion time scale  $\tau_d$  is defined by the ratio  $L^2/D$  in order to make  $K_d$  independent of any parameters of the flow. Hence,  $K_d$  gives the inverse of the diffusion constant in units of  $L^2/T_0$ .

Equation (4) is solved on a doubly periodic square domain using a second-order operator splitting (Strang splitting) approach [66] which treats separately the reaction and advection-diffusion part of Eq. (4). The advection-diffusion terms are integrated with a hybrid method, introduced by Spiegelman and Katz [67], which combines the semi-Lagrangian scheme for advection with the Crank-Nicolson algorithm for the diffusion equation. In the semi-Lagrangian method, we use a second-order midpoint iteration technique for finding the departure point of each fluid parcel at previous time step [68], together with bicubic interpolation for approximating the values of the advected fields at departure points. The bicubic interpolation is constructed from a series of one-dimensional cubic spline interpolations with fourth-order central difference estimates of the derivatives at the interpolating nodes. To reduce spurious oscillations, which typically arise from standard high-order interpolations near sharp gradients of the concentration fields, a monotonicity-preserving modification of the derivatives is used for each one-dimensional cubic interpolation [69]. The reaction terms are integrated independently of the advection-diffusion part with a second-order Runge-Kutta scheme. In order to make our numerical method consistent with the externally supplied time-dependent flow field  $\mathbf{v}(\mathbf{r},t)$ , the same spatial resolution as in the 2D turbulence simulation ( $768^2$  grid points) is used to solve Eq. (4).

In all simulations, we use initial conditions of the form

$$(a^* + \delta\xi_a, b^* + \delta\xi_b, c^* + \delta\xi_c), \quad (6)$$

where  $(a^*, b^*, c^*) = \frac{\mu}{3\mu+\sigma}(1,1,1)$  is the reactive fixed point of Eq. (2),  $\{\xi_s\}$  are randomly distributed numbers between  $-1$  and  $1$ , and  $\delta$  is the amplitude of fluctuations around the reactive fixed point. The random numbers are generated independently for each point on the computational grid so no spatial correlations are present in the initial conditions. We also avoid using the same flow time evolution for all simulation runs by initializing the random turbulence forcing term differently for each run. It is important to note that various initial conditions and flow realizations should be considered for studies of ecosystem stability because any particular solution of Eq. (4) might show stability properties that—on a given

time scale—significantly differ from the statistical average over many realizations.

### III. RESULTS

To investigate the characteristics of our spatially extended population model we performed over 250 simulation runs for the system (4). In most cases, the equations were integrated over a time  $T \approx 23\tau_r$ . In order to determine the circumstances under which the spatial degrees of freedom facilitate a significant improvement of ecosystem stability, it is sufficient to consider time scales which are only about an order of magnitude larger than  $\tau_r$ , since the heteroclinic orbits of the well-mixed system (2) typically require less than  $\tau_r$  to reach the boundaries of the phase space. In the following, we refer to the time scales which are only about an order, or perhaps a few orders, of magnitude larger than  $\tau_r$  as to the biological or ecological *time scales of interest*. Moreover, the term “long-time regime” should be in the following understood only in the context of such time scales.

In our simulations, the amplitude of fluctuations around the reactive fixed point in the initial conditions was set to  $\delta = 2.5 \times 10^{-3}$ , and we have always used equal selection and reproduction rates ( $\mu = \sigma$ ). Reichenbach *et al.* [12] have shown that different choices of the ratio  $\sigma/\mu$  do not qualitatively change the system’s dynamics in the limit  $Da \rightarrow \infty$ . It seems reasonable to expect this to be true in general for all Damköhler numbers, although we have not explicitly considered various choices of  $\sigma/\mu$  in our simulations. Different values of  $Da$  for fixed  $K_d$  were in the simulations achieved by rescaling the entire right-hand side of Eq. (4) while keeping the parameters of the flow unchanged. The same effect could have been alternatively achieved by varying the magnitude of the flow field while keeping the parameters of the reaction-diffusion part fixed.

Different aspects of the solutions are presented in two subsections. In Sec. III A we describe the spatiotemporal dynamics for those choices of  $Da$  and  $K_d$  that give rise to a heterogeneous spatial structure (i.e., the system is able to maintain a state of biodiversity). In the following, we call the latter range of values for  $Da$  and  $K_d$  the *species coexistence region*. A more formal definition of this term is given later in Sec. III B, where we discuss the transitions between different dynamical regimes and present a rough nonequilibrium phase diagram of the spatiotemporal dynamics.

#### A. System’s spatiotemporal evolution

The spatial structure of solutions can be qualitatively explored through snapshots of the subpopulation densities  $a(\mathbf{r}, t)$ ,  $b(\mathbf{r}, t)$ , and  $c(\mathbf{r}, t)$ . Figure 3 shows a selection of long-time snapshots of the solutions. In the long-time regime, the three species occupy separate parts of the (periodic) domain, forming various types of patterns which give qualitative insight into the underlying character of spatial transport. In the top row of Fig. 3, we show solutions obtained in the absence of fluid flow in order to draw a clear picture of the differences between the full set of RDA equations and the reaction-diffusion dynamics with  $\mathbf{v}(\mathbf{r}, t) = 0$ . The patterns resulting from the interplay among reactions, diffusion, and turbulent

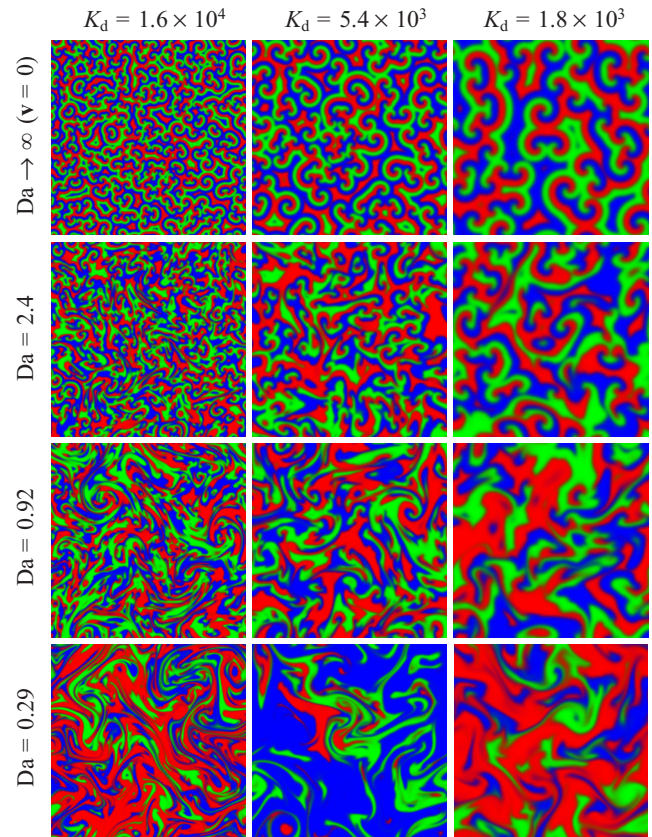


FIG. 3. (Color online) Snapshots of the concentration fields  $a$ ,  $b$ , and  $c$  for different Damköhler numbers  $Da$  and ratios of the diffusion-to-reaction-time-scale  $K_d$ . Each subpopulation density is represented by its own color channel (gray tone)—red (medium gray) for  $a$ , green (light gray) for  $b$ , and blue (dark gray) for  $c$ .

advection in general differ substantially from those induced by diffusive transport alone because the chosen flow field is correlated on the largest scale resolved by the simulations. For moderately large Damköhler numbers (Fig. 3, second row), one can observe a collection of irregular spiral shapes which are rendered unstable by the stretching and folding of material lines in 2D turbulence (see also Supplemental Material, [70] Movie 1). In other words, these spirals have a finite lifetime. However, new spirals are spontaneously formed at a similar rate as the old ones are being destroyed. For Damköhler numbers around  $Da \approx 1$  (Fig. 3, third row), the reaction-diffusion dynamics and turbulent advection are found to be in an approximate dynamic balance (Supplemental Material [70], Movie 2). This statement will be clarified later when we examine the time autocorrelation functions. As the Damköhler number is decreased even further (Fig. 3, bottom row), fluid mixing significantly increases the effective range of species’ interactions, leading to collective oscillations in relative species abundance on the largest scales (Supplemental Material [70], Movie 3). This phenomenon will be discussed in more detail later.

The influence of turbulent transport on the system’s dynamics is strongest for low  $Da$  and high  $K_d$ . In this regime, the subpopulation densities are expected to behave effectively as passive (weakly diffusive) tracers on the time scale of the flow

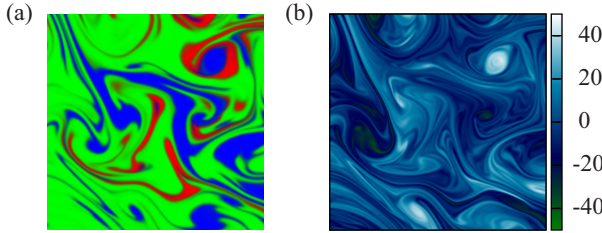


FIG. 4. (Color online) Adaptation of spatial patterns to the vorticity field structure in the regime of long reaction-diffusion time scales compared to the characteristic flow time scale. (a) Snapshot of the subpopulation densities  $a$ ,  $b$ , and  $c$ . Different colors (gray tones) should be interpreted in the same way as in Fig. 3. (b) The vorticity field of 2D turbulence. Only  $1/4$  of the whole domain is shown in (a) and (b). Both snapshots are taken at the same time of the simulation run.

$\tau_f$ , adapting a structure similar to that of the vorticity field [29]. Figure 4 compares a solution of Eq. (4) for  $Da = 0.18$  and  $K_d = 1.6 \times 10^4$  with the instantaneous vorticity field and confirms this prediction. However, on the time scale of the reaction  $\tau_r$  the concentration fields are highly sensitive to fluid mixing and develop large oscillations in relative species abundance as already mentioned above.

The most intriguing questions regarding the system's time evolution are those related to the long-time maintenance of biodiversity. In the species coexistence region, the total space-averaged density  $\bar{\rho}$  always reaches a nearly steady value close to 0.9. On the contrary, the space-averaged subpopulation densities  $\bar{a}$ ,  $\bar{b}$ , and  $\bar{c}$  never settle to a steady value but rather oscillate around their space-time average; approximately  $1/3$  of the total density. The time evolution observed for low Damköhler numbers deserves some special attention. In this regime, the space-averaged concentrations display surprisingly regular periodic oscillations, and the three subpopulations cyclically dominate the total biomass of the system (Fig. 5). A large global concentration of one of the subpopulations does not necessarily lead to a loss of biodiversity because an abundant species represents a convenient “spreading medium” for its superior competitor that can easily outperform the first species and become abundant itself before it is in turn replaced by the third species, and so on. However, when the relative strength of mixing is increased further, the amplitudes of oscillations approach the lower bound of the total space-averaged concentration  $\bar{\rho}$ , so the probability of extinction increases, until species coexistence becomes almost impossible.

Collective oscillations in cyclic competitions with fluid mixing have also been reported by Károlyi *et al.* [6]. The model studied in Ref. [6] was composed of cyclic interactions between three species and an analytically prescribed unidirectional shear flow with a changing direction. Like in our turbulence model, large-scale correlations were present in the velocity field used in Ref. [6]. Interestingly, transitions to states with global oscillations have also been observed in studies of cyclic competitions on regular small-world networks, where a given portion of randomly chosen nearest-neighbor links is replaced with long-range links [71,72]. In view of these previous works, our results provide further evidence

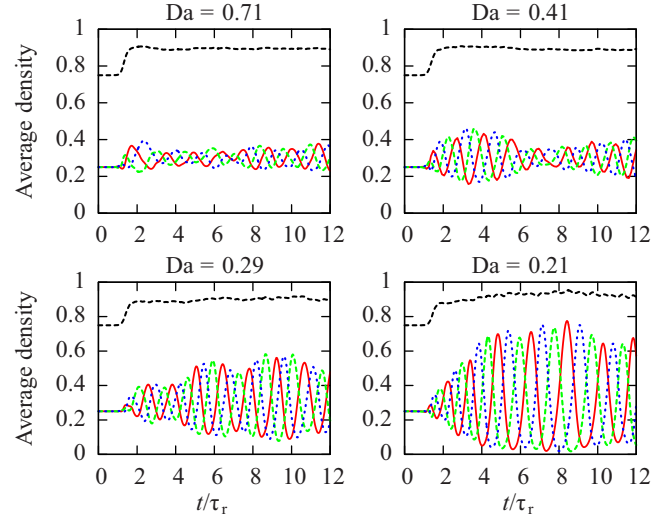


FIG. 5. (Color online) Transition to low Damköhler numbers where space-averaged concentrations display large periodic oscillations. The solid red (medium gray), dashed green (light gray), and dotted blue (dark gray) lines display the space-averaged subpopulation densities. The dashed black lines show the total space-averaged density. The diffusion-to-reaction-time-scale ratio  $K_d$  was set to  $K_d = 8.1 \times 10^3$  in all cases.

that the collective oscillations are a robust phenomenon, unaffected by the details of cyclic interactions, as long as there exists a mechanism capable of mediating interactions among spatially separated parts of the system. For sufficiently small velocity field correlation lengths in statistically stationary and homogeneous flows, however, it should be possible to approximate advection with an effective diffusion, thereby eliminating the possibility of collective oscillations. Instead, the effect of advection in this case would be to increase the size of spiral patterns observed in the absence of fluid flow. This phenomenon was recently demonstrated in experiments by von Kameke *et al.* [50] with the pattern-forming Belousov-Zhabotinsky reaction in a quasi-2D turbulent flow.

To gain a more quantitative understanding of the system's spatiotemporal dynamics, we computed the normalized space-time autocorrelation functions

$$C_{ss}(|\mathbf{r} - \mathbf{r}'|, t, t') \equiv \frac{1}{\sigma^2} \langle s(\mathbf{r}, t) s(\mathbf{r}', t') \rangle - \frac{1}{\sigma^2} \langle s(\mathbf{r}, t) \rangle \langle s(\mathbf{r}', t') \rangle, \quad (7)$$

where  $s \in \{a, b, c\}$ ,  $\sigma^2 = \langle s(\mathbf{r}, t)^2 \rangle - \langle s(\mathbf{r}, t) \rangle^2$ , and the brackets  $\langle \dots \rangle$  should be in principle understood as ensemble averages over all possible realizations of the flow and over all initial conditions. When the probability that one (or two) of the species will go extinct becomes small on any biologically reasonable time scale, the autocorrelations in the system's long-time regime may be approximated with finite-time averages. Under such circumstances, the temporal part of  $C_{ss}(|\mathbf{r} - \mathbf{r}'|, t, t')$  in the long-time regime depends only on  $|t - t'|$ . For large Damköhler numbers, the solutions of Eq. (4) strongly depend on initial conditions which raises a concern regarding the validity of approximating Eq. (7)

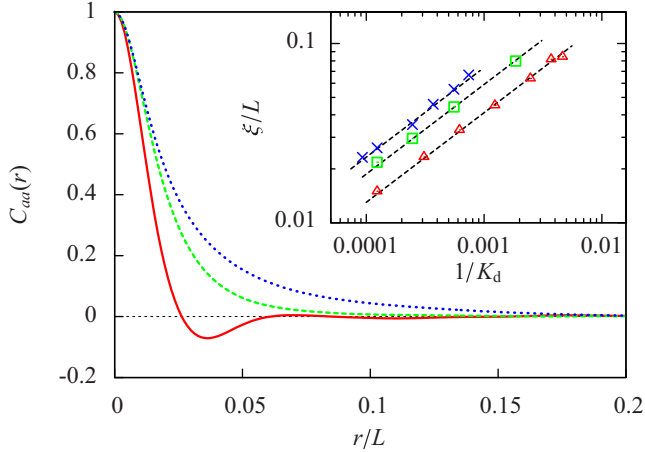


FIG. 6. (Color online) Spatial autocorrelation functions for different Damköhler numbers  $Da$ . The correlations  $C_{aa}(r)$  are shown for  $Da = 4.7$  (solid red line),  $Da = 0.92$  (dashed green line), and  $Da = 0.29$  (dotted blue line). The diffusion-to-reaction-time-scale ratio  $K_d$  was kept fixed at  $K_d = 8.1 \times 10^3$  in all cases. For higher values of  $Da$ , the autocorrelations suddenly develop a local minimum which emerges due to the presence of rotating spiral patterns. The inset shows the correlation lengths as functions of  $1/K_d$  for  $Da = 4.7$  (red triangles),  $Da = 0.92$  (green squares), and  $Da = 0.29$  (blue crosses). The dashed lines on the logarithmic graph have a slope of  $1/2$  which means that all correlation lengths scale as  $\xi \sim 1/\sqrt{K_d}$ , albeit with a different proportionality factor for each  $Da$ .

with a time average. Nevertheless, we found that various initial conditions in the form of expression (6) give very similar estimates for  $C_{ss}(|\mathbf{r} - \mathbf{r}'|, t, t')$ , even in the high- $Da$  limit. Since the ecosystem model (4) is homogeneous, the autocorrelations may also be evaluated with the help of space averages. However, space averages alone generally do not give sufficiently accurate results due to the presence of various finite-size effects in the solutions of Eq. (4).

Spatial autocorrelation functions  $C_{ss}(|\mathbf{r} - \mathbf{r}'|) \equiv C_{ss}(|\mathbf{r} - \mathbf{r}'|, t, t)$  for different choices of  $Da$  are shown in Fig. 6. The functions  $C_{ss}(|\mathbf{r} - \mathbf{r}'|)$  were calculated from a space average and an additional time average over time  $T \approx 13\tau_r$ , once the total population density had reached a steady value. In this way, we were able to obtain well-behaved estimates of  $C_{ss}(|\mathbf{r} - \mathbf{r}'|)$  with a monotonically decreasing correlation length  $\xi$  [the length  $\xi$  at which  $C_{ss}(\xi) = \exp(-1)$ ] as a function of  $Da$  and  $K_d$ . The correlation length falls with  $Da$  ( $K_d$ ) because an increase of  $Da$  ( $K_d$ ) generally corresponds to a reduced total mixing rate. It has been previously shown that  $\xi$  scales with the square root of the diffusion constant in the absence of fluid flow [12]. Our results suggest that the scaling relation  $\xi \sim \sqrt{D} \sim 1/\sqrt{K_d}$  remains valid in general for any choice of  $Da$ .

The time autocorrelations  $C_{ss}(|t - t'|) \equiv C_{ss}(0, t, t')$  were initially obtained from a time average over time  $T \approx 11\tau_r$ , taken at a fixed point inside the simulation domain, once the total density had reached a steady value. By examining the initial estimates, we realized that the chosen averaging time was too short to give satisfactory results. Therefore, we picked three points from different regions of the parameter space and improved our estimates of  $C_{ss}(|t - t'|)$ —for those

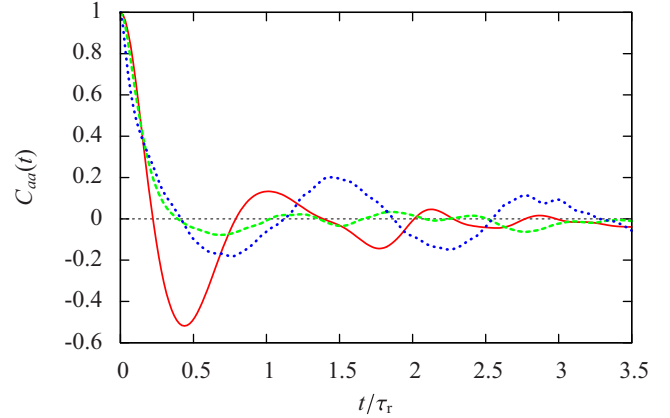


FIG. 7. (Color online) Time autocorrelation functions for different Damköhler numbers  $Da$ . Estimates of  $C_{aa}(t)$  were obtained for  $Da = 0.29$  (dotted blue line),  $Da = 0.92$  (dashed green line), and  $Da = 4.7$  (solid red line). The diffusion-to-reaction-time-scale ratio  $K_d$  was set to  $K_d = 3.2 \times 10^3$  in all cases.

three particular choices of control parameters—by taking an additional average over 15 realizations of the model. The final results for  $C_{ss}(|t - t'|)$  are shown in Fig. 7. The estimated time autocorrelations are not as well behaved as their corresponding spatial part, but we are still confident that the results in Fig. 7 are sufficiently accurate to correctly predict the gross features of the time autocorrelations. Namely,  $C_{ss}(|t - t'|)$  display damped oscillations, except for values of  $Da$  around  $Da \approx 1$ . In the low- $Da$  regime, the oscillations in  $C_{ss}(|t - t'|)$  arise from the collective oscillations in relative species abundance, whereas in the high- $Da$  regime, the oscillations result from the (unstable) rotating spiral patterns. For intermediate values of  $Da$  around  $Da \approx 1$ , the time autocorrelations quickly decay towards zero without any clear signs of (damped) oscillations. This result justifies the use of the spirals' rotation period  $T_0$  for the definition of the reaction time scale  $\tau_r$  because the reactions appear to be approximately in balance with turbulent advection when  $Da \approx 1$  (i.e., when  $T_0 \approx \tau_f$ ).

## B. Global attractors and ecosystem stability

The qualitative changes in the system's spatiotemporal dynamics with respect to the control parameters seem very pronounced, suggesting that the model's parameter space can be divided into different dynamical regimes. To develop our idea further, we follow the approach of Rulands *et al.* [51] and analyze the attractors of the global (space-averaged) dynamics. Adopting the terminology of Ref. [51], we call the attractors of the space-averaged dynamics *global attractors*. To avoid confusion, we note that the same phrase is also used in a similar context in mathematical literature but its specific meaning there differs. Due to the inherent presence of flow-induced statistical fluctuations, the global attractors correspond to maxima of the probability density to find the system in a specific global state  $(\bar{a}, \bar{b}, \bar{c})$  rather than to isolated orbits or points, for example. In this framework, the transitions between different dynamical regimes are to be interpreted as bifurcations of the global dynamics and should not be confused with nonequilibrium phase transitions. Moreover, the

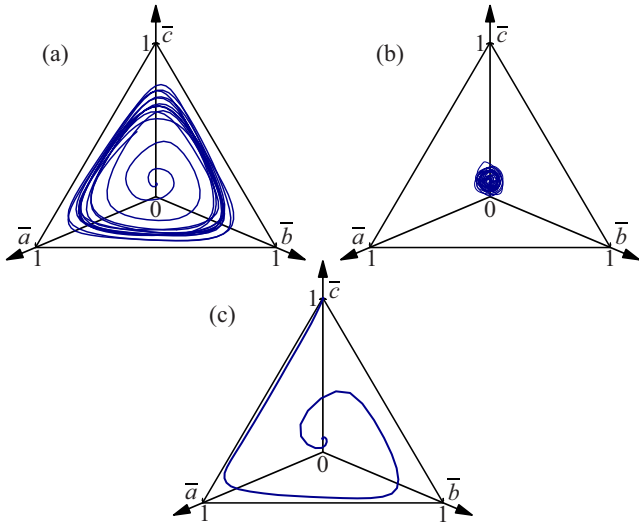


FIG. 8. (Color online) Global phase portraits of the dynamics for different Damköhler numbers  $Da$  and ratios of the diffusion-to-reaction-time-scale  $K_d$ . The trajectories of the space-averaged solutions are shown for  $Da = 0.21$ ,  $K_d = 8.1 \times 10^3$  (a);  $Da = 0.71$ ,  $K_d = 8.1 \times 10^3$  (b); and  $Da = 0.29$ ,  $K_d = 5.4 \times 10^2$  (c).

observed qualitative changes in the dynamics arise essentially from finite-size effects due to variations of the physical length scales compared to the domain size. Evidently, the global attractors do not give any information regarding the small-scale variability of the subpopulation densities. However, the dimensional reduction of the problem considerably simplifies the search for bifurcations in the parameter space, while at the same time it still gives valuable insight into the nature of biological interactions on the largest scales.

Figure 8 shows three global phase portraits of the solutions, corresponding to three different types of global attractors observed in our simulations. The attractors can be readily identified as a “limit cycle” [Fig. 8(a)], a “fixed point” [Fig. 8(b)], and a heteroclinic orbit [Fig. 8(c)]. The solutions starting in the vicinity of the reactive fixed point of Eq. (2) converge (in a statistical sense) to a limit cycle or to the fixed point attractor if turbulent mixing is not too strong so biodiversity can be maintained on the time scales of interest. It is worth emphasizing that the fixed point global attractor does not coincide with the reactive fixed point of the rate equations. Instead, it is shifted along the symmetry axis  $\bar{a} = \bar{b} = \bar{c}$  towards a higher density  $\bar{\rho} \approx 0.9$  as compared to

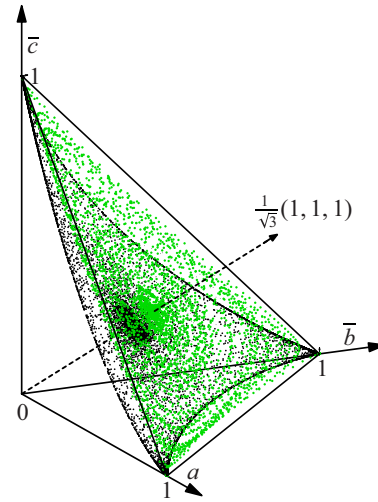


FIG. 10. (Color online) The invariant manifold of Eq. (2) (black dots) compared to the solutions of Eq. (4) projected onto the global phase space [green (gray) dots]. The dashed arrow denotes the unit vector along the symmetry axis.

the well-mixed limit where  $\rho = 3/4$  in the reactive fixed point. The limit cycle global attractors correspond to oscillations in relative species abundance observed for low  $Da$ . In the context of dynamical systems theory, the collective oscillations are quite a remarkable property, considering the fact that the well-mixed system (2) is characterized by heteroclinic orbits rather than by limit cycles. Neglecting the mathematical details regarding the true asymptotic nature of solutions corresponding to heteroclinic orbits, we may say that the heteroclinic orbits correspond to extinctions of all but one species. In the spatially extended model (4), the system tends to get trapped into one of the absorbing states when the average size of spatial patterns approaches the domain size (Fig. 9). The size of spatial patterns is, in turn, controlled by  $Da$  and  $K_d$ . Therefore, species coexistence depends essentially on the choice of  $Da$  and  $K_d$ .

A common feature shared by all global attractors of the spatially extended model is their confinement to a quasi-2D geometry within the three-dimensional global phase space. In Fig. 10, we show the projections of long-time solutions for various  $Da$  and  $K_d$  onto the global phase space and compare the obtained result with the invariant manifold of Eq. (2). It is shown that the global dynamics can be effectively reduced

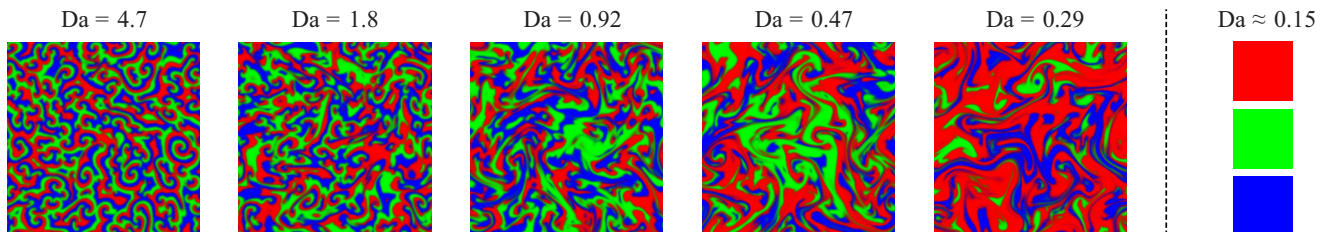


FIG. 9. (Color online) Approach to the absorbing state with a decreasing Damköhler number  $Da$  at a fixed diffusion-to-reaction-time-scale ratio  $K_d = 8.1 \times 10^3$ . Each subpopulation density is represented by its own color channel (gray tone) as described in Fig. 3. As illustrated above, a relative increase of turbulent advection enhances the dispersal of species and increases the average size of spatial patterns until the biodiversity is lost. For  $K_d = 8.1 \times 10^3$ , we were able to observe the first extinction events around  $Da \approx 0.15$ .

to a quasi-2D surface within the global phase space which does not correspond to the invariant manifold of Eq. (2). The quasi-2D surface spanned by the solutions of Eq. (4) has a very mild curvature at the intersection with the symmetry axis around  $\bar{\rho} \approx 0.9$  and becomes slightly more curved close to the boundaries of the phase space where it touches the single-species equilibrium points. For most values of  $Da$  and  $K_d$  considered in our simulations, even the solutions that correspond to transitions into absorbing states lie on this surface rather than on the invariant manifold of the well-mixed system. A significant departure of the phase portraits from the global surface of solutions was observed only for  $K_d \sim 10$ , and it should be probably required that  $K_d \sim 1$  in order to completely neglect the spatial degrees of freedom.

Let us now try to analyze the transition into the collective oscillations regime in more detail. Due to the inherent presence of noise in the system, it is necessary to use a statistical approach to distinguish between the fixed point and limit cycle global attractor. In order to distinguish a limit cycle from small fluctuations around the symmetry axis which correspond to the fixed point attractor, the global trajectories have to be well separated from the symmetry axis  $\bar{a} = \bar{b} = \bar{c}$ . To introduce a measure for the mean separation of trajectories from the symmetry axis, we can make use of the Lyapunov function of the global concentrations  $\mathcal{L} \equiv (\bar{a}\bar{b}\bar{c})/(\bar{a} + \bar{b} + \bar{c})^3$ , which can be regarded as a radial coordinate, measuring the distance of a point from the boundaries of the global phase space [51,53]. Using the Lyapunov function, an effective radius of a limit cycle as measured from the symmetry axis can be defined as  $\mathcal{R} \equiv 1 - \mathcal{L}/\mathcal{L}_{\max}$ , where  $\mathcal{L}_{\max} = 1/27$ . Hence, to distinguish a fixed point from a limit cycle in a statistical sense, we should at least require that  $\mathcal{R}/\sqrt{\chi} \gtrsim 1$  in the collective oscillations regime, where  $\chi = \langle \mathcal{R}^2 \rangle - \langle \mathcal{R} \rangle^2$ . The dependence of the rescaled radius  $\mathcal{R}/\sqrt{\chi}$  on  $Da$  is shown in Fig. 11. The abrupt jump around  $Da_c \approx 0.4$  reflects the underlying

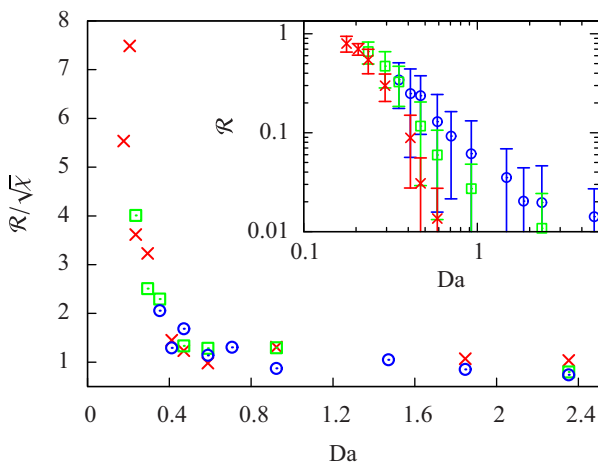


FIG. 11. (Color online) Dependence of the rescaled radius  $\mathcal{R}/\sqrt{\chi}$  on the Damköhler number  $Da$  for different diffusion-to-reaction-time-scale ratios  $K_d$ . Estimates of  $\mathcal{R}/\sqrt{\chi}$  are shown for  $K_d = 8.1 \times 10^3$  (red crosses),  $K_d = 1.8 \times 10^3$  (green squares), and  $K_d = 5.4 \times 10^2$  (blue circles). The inset shows the measurements of  $\mathcal{R}$  with the error bars representing the magnitude of statistical fluctuations  $\sqrt{\chi}$ .

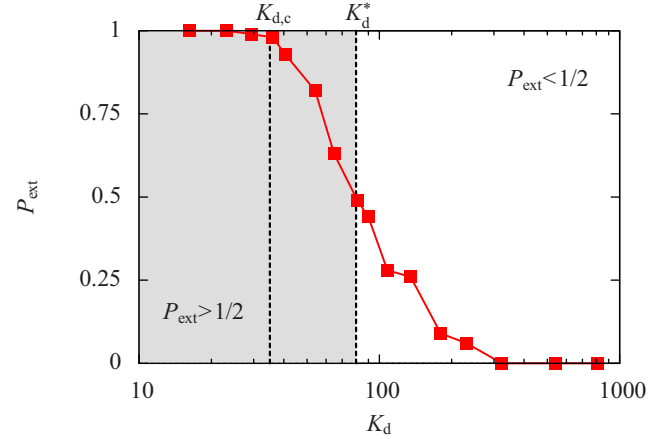


FIG. 12. (Color online) Extinction probability  $P_{\text{ext}}$  calculated in the absence of fluid flow as a function of the diffusion-to-reaction-time-scale ratio  $K_d$ . The values  $K_{d,c}$  and  $K_d^*$  on the graph denote the points above which the extinction probability drops below  $P_{\text{ext}} \approx 1$  and  $P_{\text{ext}} \approx 1/2$ , respectively.

bifurcation of the global dynamics. We do not rule out a possible weak dependence of the transition also on  $K_d$ , but the available simulation data are insufficient to clearly confirm or neglect a possible dependence on  $K_d$ .

To quantitatively describe the transitions into absorbing states, one can consider the extinction probability  $P_{\text{ext}}$  that two species have gone extinct after time  $T$  [7]. For the sake of simplicity, and for consistency with previous works [7,51] performed for the discretized version of model (4) in the absence of fluid flow, let us first discuss the limiting case  $Da \rightarrow \infty$ . To begin with, the meaning of the extinction probability in deterministic reaction-diffusion models requires some special attention. The randomness in discrete models originates from the stochastic nature of biological interactions, whereas in models described by partial differential equations (PDEs) the “randomness” can be achieved by considering various initial conditions. These two formulations might at a first glance appear as completely unrelated; however, our approach illustrates that the results of the PDE model are equivalent to the ones produced from discrete lattice simulations with a large number of particles [7,12], provided that the initial conditions match the solutions of the discrete lattice model at early stages of the system’s time evolution. In our case, this means that the initial conditions for the PDE model should be generated as random,  $\delta$ -correlated-in-space perturbations around the reactive fixed point of Eq. (2). In Fig. 12, we show the dependence of  $P_{\text{ext}}$  on  $K_d$  in the limit  $Da \rightarrow \infty$ . Since the spatial patterns of the reaction-diffusion system remain unchanged for all times after an initial transient of a typical duration  $T \sim 10\tau_r$ , we consider a waiting time  $T \approx 9.8\tau_r$ , and each estimate for  $P_{\text{ext}}$  is obtained from an average over 100 initial conditions. The critical value  $K_{d,c} = 35 \pm 5$ , below which species coexistence becomes almost impossible, is in good agreement with the result from Reichenbach *et al.* [7] obtained from discrete lattice simulations (written in terms of  $K_d$ , the estimate from Ref. [7] reads  $K_{d,c} = 36 \pm 4$ ).

A large number of simulations are required for an accurate estimate of the threshold  $K_{d,c}$  because the survivals of all

three competitors are statistically very rare near  $K_{d,c}$ . If one only requires rough estimates of the transition points into the absorbing states, a better alternative is to consider a threshold  $K_d^*$  for which  $P_{\text{ext}} \approx 1/2$  (see Fig. 12). Indeed, rough estimates of  $K_d^*$  can be obtained even if only a single simulation run is performed for each choice of the control parameters because the point  $K_d^*$  should be in any case bounded from above by the values of  $K_d$  for which  $P_{\text{ext}} \approx 0$  and from below by those values for which  $P_{\text{ext}} \approx 1$ . Therefore, in order to spend our computational resources wisely, we have not explicitly considered the extinction probabilities for the more general case of a nonzero fluid velocity since it is already possible to make qualitative conclusions regarding ecosystem stability from a very limited number of simulation runs, performed for various choices of  $Da$  and  $K_d$ . For the reasons explained above, we use the threshold  $P_{\text{ext}} \approx 1/2$  as a more formal definition of the boundary between the species coexistence region and the extinction region. It should be emphasized that in the presence of random fluctuations, such as the ones arising from a turbulent flow, the ecosystem can never remain stable in the strict limit  $T \rightarrow \infty$  because there always exists a possibility that the random disturbances will drive the system into one of its absorbing states. The global attractors from the species coexistence region are therefore in a strict mathematical sense only long-lived transients. However, for sufficiently large  $K_d$  and  $Da$  the extinction probability becomes very small on the biological time scales of interest, and the states corresponding to these parameters may be for practical purposes regarded as states of species coexistence [73].

To determine the relative extent of the species coexistence region in the parameter space, we performed several simu-

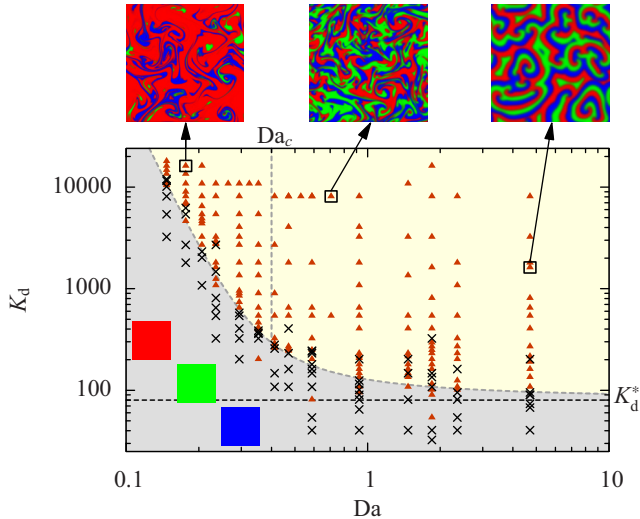


FIG. 13. (Color online) Nonequilibrium phase diagram of the spatiotemporal dynamics. The black crosses show the simulation runs where biodiversity was lost before  $T \approx 23\tau_r$ , and the brown triangles show the survivals of all three species. The (medium) gray shading indicates the region of extinction where transitions into absorbing states become more probable than long-lived states of biodiversity. The horizontal and vertical dashed lines show the thresholds  $K_d^*$  and  $Da_c$ , respectively (see text for further details). Above the phase diagram we show three long-time snapshots of the solutions from different parts of the species coexistence region.

lations for various  $Da$  and  $K_d$ . In each of these simulations we integrated Eq. (4) for at least  $T \approx 23\tau_r$ . Figure 13 finally summarizes the main global dynamical features of our spatially extended ecosystem with a nonequilibrium phase diagram. Based on how the species extinction events and their survivals are distributed across the parameter space, it is possible to sketch a rough dependence of the  $P_{\text{ext}} \approx 1/2$  extinction probability threshold on  $Da$  and  $K_d$ . Below the transition into the collective oscillations regime around  $Da_c$ , the turbulent flow becomes increasingly capable of synchronizing the local subpopulation density oscillations among distant parts of the domain, which in turn greatly reduces the extent of the species coexistence region with respect to  $K_d$ . For high  $Da$ , our results seem to be consistent with the limiting value  $K_d^*$ , estimated from the simulations performed in the absence of fluid flow.

#### IV. CONCLUSIONS

We studied the population dynamics of three cyclically competing species in a two-dimensional turbulent flow forced at large scales. The presented results of our numerical simulations give new insight into how turbulent transport affects ecosystem structure in biological communities without a clear competition hierarchy. More specifically, we performed simulations over a broad range of relative advection and diffusion strengths compared to the biological reactions and studied how different choices of ecosystem parameters affect the system's spatiotemporal dynamics and species' biodiversity. For short reaction time scales  $\tau_r$  compared to the characteristic flow time scale  $\tau_f$ , corresponding to large Damköhler numbers  $Da = \tau_f/\tau_r$ , the subpopulations self-organize into rotating spiral waves. This phenomenon is consistent with previous studies of cyclic competitions in reaction-diffusion systems, with the exception that the spiral patterns become unstable when subjected to perturbations induced by a turbulent flow. For Damköhler numbers around  $Da \approx 1$ , with  $\tau_r$  defined as the spirals' rotation period measured in the absence of fluid flow, the reaction-diffusion dynamics and turbulent advection are found to be in an approximate dynamic balance. This is most clearly seen by inspecting the species (Eulerian) time autocorrelation functions, which do not show any clear signs of periodic oscillations for  $Da \approx 1$ . When the Damköhler number is decreased even further, a sharp transition to a state with collective oscillations in relative species abundance is observed at a certain threshold value of  $Da$ . The observed phenomenon suggests that turbulence might play an important role in the structuring of marine phytoplankton communities, which are typically composed of only a few dominant species while the remaining ones represent only a small fraction of the total biomass [74]. These types of interpretations are also supported by some recent numerical experiments presented in Ref. [75].

To further investigate the transitions between the qualitatively different dynamical regimes observed in our simulations, we studied the attractors of the global (space-averaged) dynamics and identified three different types attractors, corresponding to maxima of the probability density to find the system in a specific global (space-averaged) state. The three different types of global attractors have been identified as a

fixed point, limit cycles, and heteroclinic orbits. The transitions among these attractors should be interpreted as bifurcations of the global dynamics. The fixed point attractor corresponds to states of species coexistence observed for Damköhler numbers of order unity and above, whereas the limit cycles correspond to collective oscillations observed for low  $Da$ . The heteroclinic orbits indicate transitions to homogeneous states, where the system's biodiversity is lost. The probability that two of the species will go extinct depends essentially on the choice of ecosystem parameters. Outside the regime of collective oscillations, the extinction probability depends most strongly on the relative strength of diffusion compared to the reactions. However, as the Damköhler number drops below a certain threshold, turbulence becomes increasingly capable of synchronizing oscillations among distant parts of the domain, which greatly reduces the acceptable range of relative diffusion strengths that still allow for species coexistence.

In all of our simulations, we used the same type of turbulent flow. Further studies could investigate the effects of different types of flows on cyclic interactions and identify which system properties are more general and which ones depend on the details of the turbulence model. In particular, it would be interesting to consider the dependence of solutions on the correlation length of the flow, since it would seem reasonable to expect that the turbulent flow becomes incapable of producing collective oscillations in relative species abundance when the

correlation length is much smaller than the domain size. To shed some light on these speculations, we performed a couple of trial simulations at  $\ell_f = L/10$ . There, we were still able to observe the collective oscillations but their amplitude for the same choice of  $Da$  was somewhat smaller.

Finally, it should also be noted that even though the main motivation for this work comes from the field of theoretical population biology, the presented results are also relevant in other fields where RDA systems of a similar type as the one studied here can be found. In particular, pattern-forming reactions in fluid flows have also been realized in experiments with the chemical Belousov-Zhabotinsky reaction [32,49,50]. See Ref. [76] for information regarding the project's source code.

#### ACKNOWLEDGMENTS

The research leading to these results has received funding from the European Research Council under the European Union's Seventh Framework Programme (FP7/2007-2013)/ERC Grant Agreement No. 277870. This research was also supported by the German Excellence Initiative via the program "Nanosystems Initiative Munich" and the Deutsche Forschungsgemeinschaft via Contract No. FR 850/9-1. We thank V. Bratanov, K. Reuter, T. Görler, and E. Sonnendrücker for useful discussions. We also thank M. Perc for comments on the manuscript.

- 
- [1] R. Durrett and S. Levin, *J. Theor. Biol.* **185**, 165 (1997).
  - [2] R. Durrett and S. Levin, *Theor. Popul. Biol.* **53**, 30 (1998).
  - [3] A. Bracco, A. Provenzale, and I. Scheuring, *Proc. R. Soc. Lond. B* **267**, 1795 (2000).
  - [4] M. Frean and E. R. Abraham, *Proc. R. Soc. Lond. B* **268**, 1323 (2001).
  - [5] B. Kerr, M. A. Riley, M. W. Feldman, and B. J. M. Bohannan, *Nature (London)* **418**, 171 (2002).
  - [6] G. Károlyi, Z. Neufeld, and I. Scheuring, *J. Theor. Biol.* **236**, 12 (2005).
  - [7] T. Reichenbach, M. Mobilia, and E. Frey, *Nature (London)* **448**, 1046 (2007).
  - [8] W.-X. Wang, X. Ni, Y.-C. Lai, and C. Grebogi, *Phys. Rev. E* **83**, 011917 (2011).
  - [9] K. I. Tainaka, *Phys. Rev. Lett.* **63**, 2688 (1989).
  - [10] L. Frachebourg, P. L. Krapivsky, and E. Ben-Naim, *Phys. Rev. Lett.* **77**, 2125 (1996).
  - [11] M. Perc and A. Szolnoki, *New J. Phys.* **9**, 267 (2007).
  - [12] T. Reichenbach, M. Mobilia, and E. Frey, *J. Theor. Biol.* **254**, 368 (2008).
  - [13] Q. He, M. Mobilia, and U. C. Täuber, *Phys. Rev. E* **82**, 051909 (2010).
  - [14] J. Juul, K. Sneppen, and J. Mathiesen, *Phys. Rev. E* **85**, 061924 (2012).
  - [15] A. Roman, D. Konrad, and M. Pleimling, *J. Stat. Mech.* (2012) P07014.
  - [16] P. P. Avelino, D. Bazeia, L. Losano, J. Menezes, and B. F. Oliveira, *Phys. Rev. E* **86**, 036112 (2012).
  - [17] A. Szolnoki, M. Mobilia, L.-L. Jiang, B. Szczesny, A. M. Rucklidge, and M. Perc, *J. R. Soc. Interface* **11**, 20140735 (2014).
  - [18] A. P. Martin, *Prog. Oceanogr.* **57**, 125 (2003).
  - [19] C. Pasquero, A. Bracco, and A. Provenzale, in *Shallow Flows*, edited by G. H. Jirka and W. S. J. Uijtewaal (Balkema, Leiden, 2004).
  - [20] M. Lévy, *Lect. Notes Phys.* **744**, 219 (2008).
  - [21] J. Huisman and F. J. Weissing, *Ecology* **82**, 2682 (2001).
  - [22] A. D. Barton, S. Dutkiewicz, G. Flierl, J. Bragg, and M. J. Follows, *Science* **327**, 1509 (2010).
  - [23] S. M. Burrows, T. Butler, P. Jöckel, H. Tost, A. Kerkweg, U. Pöschl, and M. G. Lawrence, *Atmos. Chem. Phys.* **9**, 9281 (2009).
  - [24] A. M. Womack, B. J. M. Bohannan, and J. L. Green, *Phil. Trans. R. Soc. B* **365**, 3645 (2010).
  - [25] N. DeLeon-Rodriguez, T. L. Latham, L. M. Rodriguez-R, J. M. Barazesh, B. E. Anderson, A. J. Beyersdorf, L. D. Ziemba, M. Bergin, A. Nenes, and K. T. Konstantinidis, *Proc. Natl. Acad. Sci. USA* **110**, 2575 (2013).
  - [26] I. R. Epstein, *Nature (London)* **374**, 321 (1994).
  - [27] E. R. Abraham, C. S. Law, P. W. Boyd, S. J. Lavender, M. T. Maldonado, and A. R. Bowie, *Nature (London)* **407**, 727 (2000).
  - [28] I. Kozsalka, A. Bracco, C. Pasquero, and A. Provenzale, *Theor. Popul. Biol.* **72**, 1 (2007).
  - [29] Z. Neufeld and E. Hernández-García, *Chemical and Biological Processes in Fluid Flows* (Imperial College Press, London, 2010).
  - [30] Z. Neufeld, P. H. Haynes, and T. Tél, *Chaos* **12**, 426 (2002).

- [31] Z. Neufeld, I. Z. Kiss, C. Zhou, and J. Kurths, *Phys. Rev. Lett.* **91**, 084101 (2003).
- [32] M. S. Paoletti, C. R. Nugent, and T. H. Solomon, *Phys. Rev. Lett.* **96**, 124101 (2006).
- [33] Z. Neufeld, *Chaos* **22**, 037102 (2012).
- [34] B. Sinervo and C. M. Lively, *Nature (London)* **380**, 240 (1996).
- [35] C. E. Paquin and J. Adams, *Nature (London)* **306**, 368 (1983).
- [36] B. C. Kirkup and M. A. Riley, *Nature (London)* **428**, 412 (2004).
- [37] M. F. Weber, G. Poxleitner, E. Heibisch, E. Frey, and M. Opitec, *J. R. Soc. Interface* **11**, 20140172 (2014).
- [38] A. Bracco, S. Clayton, and C. Pasquero, *J. Geophys. Res.* **114**, C02001 (2009).
- [39] K. J. Richards and S. J. Brentnall, *J. Theor. Biol.* **238**, 340 (2006).
- [40] P. Perlekar, R. Benzi, D. R. Nelson, and F. Toschi, *Phys. Rev. Lett.* **105**, 144501 (2010).
- [41] R. Benzi, M. H. Jensen, D. R. Nelson, P. Perlekar, S. Pigolotti, and F. Toschi, *Eur. Phys. J. Spec. Top.* **204**, 57 (2012).
- [42] W. M. Durham, E. Climent, M. Barry, F. De Lillo, G. Boffetta, M. Cencini, and R. Stocker, *Nat. Commun.* **4**, 2148 (2013).
- [43] E. R. Abraham, *Nature (London)* **391**, 577 (1998).
- [44] W. J. McKiver and Z. Neufeld, *Phys. Rev. E* **79**, 061902 (2009).
- [45] W. J. McKiver and Z. Neufeld, *Phys. Rev. E* **83**, 016303 (2011).
- [46] T. Ishikawa, *J. R. Soc. Interface* **6**, 815 (2009).
- [47] J. Gachelin, A. Rousselet, A. Lindner, and E. Clement, *New J. Phys.* **16**, 025003 (2014).
- [48] M. C. Cross and P. C. Hohenberg, *Rev. Mod. Phys.* **65**, 851 (1993).
- [49] C. R. Nugent, W. M. Quarles, and T. H. Solomon, *Phys. Rev. Lett.* **93**, 218301 (2004).
- [50] A. von Kameke, F. Huhn, A. P. Muñuzuri, and V. Pérez-Muñuzuri, *Phys. Rev. Lett.* **110**, 088302 (2013).
- [51] S. Rulands, A. Zielinski, and E. Frey, *Phys. Rev. E* **87**, 052710 (2013).
- [52] R. M. May and W. J. Leonard, *SIAM J. Appl. Math.* **29**, 243 (1975).
- [53] J. Hofbauer and K. Sigmund, *Evolutionary Games and Population Dynamics* (Cambridge University Press, Cambridge, 1998).
- [54] E. Frey, *Physica A* **389**, 4265 (2010).
- [55] R. Salmon, *Lectures on Geophysical Fluid Dynamics* (Oxford University Press, Oxford, 1998).
- [56] S. D. Danilov and D. Gurarie, *Phys.-Usp.* **43**, 863 (2000).
- [57] R. Kraichnan, *Phys. Fluids* **10**, 1417 (1967).
- [58] P. A. Davidson, *Turbulence* (Oxford University Press, Oxford, 2004).
- [59] G. Boffetta and R. E. Ecke, *Annu. Rev. Fluid Mech.* **44**, 427 (2012).
- [60] E. Lindborg and K. Alvelius, *Phys. Fluids* **12**, 945 (2000).
- [61] A. Bracco, J. von Hardenberg, A. Provenzale, J. B. Weiss, and J. C. McWilliams, *Phys. Rev. Lett.* **92**, 084501 (2004).
- [62] A.-K. Kassam and L. N. Trefethen, *SIAM J. Sci. Comput.* **26**, 1214 (2005).
- [63] K. Alvelius, *Phys. Fluids* **11**, 1880 (1999).
- [64] G. Boffetta and S. Musacchio, *Phys. Rev. E* **82**, 016307 (2010).
- [65] T. Reichenbach, M. Mobilia, and E. Frey, *Phys. Rev. Lett.* **99**, 238105 (2007).
- [66] W. Hundsdorfer and J. G. Verwer, *Numerical Solution of Time-Dependent Advection-Diffusion-Reaction Equations*, Springer Series in Comput. Math. 33 (Springer, Berlin, 2003).
- [67] M. Spiegelman and R. F. Katz, *Geochem. Geophys. Geosyst.* **7**, Q04014 (2006).
- [68] A. Staniforth and J. Côté, *Mon. Weather Rev.* **119**, 2206 (1991).
- [69] F. N. Fritsch and R. E. Carlson, *SIAM J. Numer. Anal.* **17**, 238 (1980).
- [70] See Supplemental Material at <http://link.aps.org/supplemental/10.1103/PhysRevE.91.033009> for movies of the system's spatiotemporal evolution.
- [71] G. Szabó, A. Szolnoki, and R. Izsák, *J. Phys. A* **37**, 2599 (2004).
- [72] C. Rulquin and J. J. Arenzon, *Phys. Rev. E* **89**, 032133 (2014).
- [73] A. Hastings, *Trends Ecol. Evol.* **19**, 39 (2004).
- [74] T. Pommier, B. Canbäck, L. Riemann, K. H. Boström, K. Simu, P. Lundberg, A. Tunlid, and Å. Hagström, *Mol. Ecol.* **16**, 867 (2007).
- [75] M. Lévy, O. Jahn, S. Dutkiewicz, and M. J. Follows, *Limnol. Oceanogr. Fluids and Environments* **4**, 67 (2014).
- [76] The simulation source code used in this study is publicly available at <https://github.com/dgroselj/DRASLA>.